Mon. Not. R. Astron. Soc. **334,** 819–832 (2002)

Hydrodynamical simulations of the stream–core interaction in the slow merger of massive stars

N. Ivanova,[1]★ Ph. Podsiadlowski[1] and H. Spruit[2]

[1]*University of Oxford, Department of Astrophysics, Oxford OX1 3RH*
[2]*Max-Planck-Institut für Astrophysik, Karl-Schwarzschild-Strasse 1, 85741 Garching, Germany*

Accepted 2002 March 27. Received 2002 March 18; in original form 2001 October 23

ABSTRACT

We present detailed simulations of the interaction of a stream emanating from a mass-losing secondary with the core of a massive supergiant in the slow merger of two stars inside a common envelope. The dynamics of the stream can be divided into a ballistic phase, starting at the L_1 point, and a hydrodynamical phase, where the stream interacts strongly with the core. Considering the merger of a 1- and 5-$M_\odot$ star with a 20-$M_\odot$ evolved supergiant, we present two-dimensional hydrodynamical simulations using the PROMETHEUS code to demonstrate how the penetration depth and post-impact conditions depend on the initial properties of the stream material (e.g. entropy, angular momentum, stream width) and the properties of the core (e.g. density structure and rotation rate). Using these results, we present a fitting formula for the entropy generated in the stream–core interaction and a recipe for the determination of the penetration depth based on a modified Bernoulli integral.

Key words: hydrodynamics – nuclear reactions, nucleosynthesis, abundances – binaries: close.

1 INTRODUCTION

A large fraction of massive stars are known to be members of binary systems which are close enough to interact strongly via Roche-lobe overflow (see e.g. Garmany, Conti & Massey 1980). One of the most dramatic, but poorly understood types of binary interactions involves the complete merger of the two components inside a common envelope which leads to the formation of a single, rapidly rotating star, possibly with some highly unusual properties. This type of evolution generally occurs as the result of dynamical mass transfer (Paczyński & Sienkiewicz 1972) where a more massive star (usually a giant) overfills its Roche lobe by an ever-increasing amount, leading to mass transfer on a dynamical time-scale. As the companion is only able to accrete matter on its thermal time-scale, most of the excess matter is believed to form a common envelope engulfing both the mass donor and the secondary. Inside this envelope, the core of the giant and the secondary form a close binary. Friction between this immersed binary and the envelope then causes the orbit to shrink. If the energy released in the process is sufficient to eject the envelope, this leads to the formation of a very close binary consisting of the core of the giant and a largely unperturbed companion star (Paczyński 1976; Taam & Sandquist 2000). However, if the envelope is not ejected in the early rapid spiral-in phase, this phase is followed by a phase of self-regulated spiral-in where all the frictional energy deposited in the envelope can be transported to the surface where it is being radiated away (Meyer & Meyer-Hofmeister 1979; Podsiadlowski 2001). For a massive primary with a mass of $\sim$20 $M_\odot$ filling its Roche lobe as a red supergiant after the end of helium core burning, the characteristic time-scale for the self-regulated spiral-in phase is several 100 yr. However, at some point, the spiraling-in secondary itself will fill its critical tidal lobe and start to transfer mass to the core of the giant. This situation is in many respects similar to the case of normal mass transfer by Roche-lobe overflow except for several fundamental differences. (i) Mass transfer occurs inside a low-density, opaque envelope, where the density contrast between the envelope and the average density of the secondary may be as high as 1:10^6. (ii) The mechanism for driving mass transfer is orbital angular momentum loss due to the friction of the immersed binary with the envelope. Because of the short spiral-in time-scale, this leads to extremely high mass-transfer rates of order 0.01–10 $M_\odot$ yr^{-1}. (iii) As the spiral-in time-scale is much shorter than a typical synchronization time-scale in a radiative star (e.g. Zahn 1975), the spin of the secondary may not be synchronized with the orbit.

As a result of this interaction, the secondary is gradually being dissolved inside the common envelope. Even though the time-scale for this dissolution is short compared to the evolutionary time-scale of a giant, it is still much longer than the dynamical time-scale of the secondary. We therefore refer to this process as a 'slow merger' of the components, although we note that this phase is likely to be terminated by a delayed dynamical instability when the flat-entropy core of the secondary is being exposed and mass transfer becomes catastrophic. This will ultimately lead to the dynamical disruption of the remnant core (if it is relatively unevolved).

In this paper we present the first part of a systematic study of the slow merger of massive stars, concentrating on the interaction of the

★E-mail: nata@northwestern.edu

mass stream emanating from the mass-losing immersed star with the core of the giant. This stream will generally not intersect with itself to form an accretion disc, but will instead penetrate deep into the core of the giant before it is stopped by the increasing pressure inside the core. As we will show, the stream may be able to reach a radius as small as $\sim 10^{10}$ cm. Because this is deep inside the hydrogen-exhausted helium core of a 20-$M_\odot$ star that has already exhausted helium in the core, this may have important consequences: (i) it can lead to the dredge-up of helium from the core which can then be mixed with the rest of the envelope, and (ii) because the material in the stream is hydrogen-rich and is heated to temperatures as high as several 10^8 K in the post-impact region, it can lead to some unusual nucleosynthesis, in particular s-processing. How deep the stream can penetrate depends not only on the initial entropy of the stream material, but also its initial angular momentum and most importantly on the structure near the core and the amount of entropy generated in the interaction with the core. It is the purpose of this paper to systematically explore how the penetration depends on these various factors and to determine the properties of the post-impact material. In a subsequent paper, we will use these results to model the slow merger of two massive stars in the context of the progenitor of SN 1987A, whose highly anomalous properties are likely the result of such a merger (see Podsiadlowski 1992,1997, for discussion and references). While the hydrodynamical simulations presented in this paper were designed with this application in mind, our analysis is sufficiently general to be applicable to other systems that have been suggested to be post-merger objects (e.g. V Hydrae, Kahane et al. 1996); FK Comae stars (e.g. Rucinski 1990; Welty & Ramsey 1994).

In Section 2 we outline the basic assumptions for modelling the initial properties of the stream leaving the mass-losing secondary. In Section 3 we use this model to obtain a description of the stream at the start of the hydrodynamical simulations. Section 4 provides a description of the numerical method used in the hydrodynamical calculations. In Section 5 we present the results of detailed hydrodynamical simulations and systematically discuss the physics of the interaction between the jet and the ambient matter, in particular the mechanism of the stream dissipation, and of rotation and nuclear burning in the stream. Finally, in Section 6 we present a semi-empirical prescription which allows one to estimate the penetration depth, taking into account the entropy generated in the interaction.

2 THE INITIAL CONDITIONS OF THE STREAM

2.1 Mass-loss rates

Once the immersed secondary starts to fill its tidal lobe, it starts to transfer mass to the core of the giant. The mass-transfer rate is determined by the friction between the spiraling-in immersed binary and the envelope which drives the evolution of the system. Because the mass-loss time-scale is generally much shorter than the nuclear or thermal time-scale for a main-sequence star, the radius responds adiabatically to mass loss, i.e.

$$\frac{\dot{R}_2}{R_2} = \left(\frac{\partial \ln R_2}{\partial \ln M_2}\right)_{\rm ad} \frac{\dot{M}_2}{M_2} \equiv \zeta_{\rm ad} \frac{\dot{M}_2}{M_2}, \tag{1}$$

where R_2 and M_2 are the radius and the mass of the mass-losing secondary, respectively.

The temporal change of the Roche-lobe radius $R_{\rm RL}$ of the secondary due to the decay of the orbit and due to the mass transfer can be written as

$$\frac{\dot{R}_{\rm RL}}{R_{\rm RL}} = \left(\frac{\partial \ln R_{\rm RL}}{\partial \ln M_2}\right)_{D=\rm const} \frac{\dot{M}_2}{M_2} + \left(\frac{\partial \ln R_{\rm RL}}{\partial t}\right)_{\dot{M}_2=0} \equiv \zeta_{\rm RL} \frac{\dot{M}_2}{M_2} + \left(\frac{\partial \ln D}{\partial t}\right)_{\dot{M}_2=0}, \tag{2}$$

where the Roche-lobe radius $R_{\rm RL}$ is given by Eggleton (1983) as

$$R_{\rm RL} = \frac{0.49\, q^{2/3}}{0.6\, q^{2/3} + \ln(1+q^{1/3})} D. \tag{3}$$

Here $q = M_2/M_1$ is the mass ratio, and M_1 is the total mass of the primary core within the binary separation D.

Assuming that the radius of the star is equal to the Roche-lobe radius, we can equate equations (1) and (2) and obtain an estimate for the mass-loss rate from the secondary as

$$\frac{\dot{M}_2}{M_2} = \frac{1}{\zeta_{\rm ad} - \zeta_{\rm RL}} \left(\frac{\partial \ln D}{\partial t}\right)_{\dot{M}_2=0}, \tag{4}$$

where $\partial \ln D/\partial t$ is the change in the orbital separation due to tidal and viscous friction. For typical conditions in a 20 $M_\odot$ supergiant, the resulting mass-loss rates are typically in the range of 0.01–10 $M_\odot\ {\rm yr}^{-1}$ (Ivanova, Podsiadlowski & Spruit 2001 and Ivanova & Podsialowski, in preparation, hereafter IP). To obtain values for $\zeta_{\rm ad}$, we performed separate stellar-evolution calculations, where mass was taken off the assumed secondary on a time-scale much shorter than the thermal time-scale in its outer envelope (see e.g. Podsiadlowski, Rappaport & Pfahl 2002).

2.2 The stream density profile and the stream width

Because of the high mass-loss rates expected in our problem, the radiative diffusion time-scale is generally much longer than the characteristic flow time-scale (for a stream with a radius of 10^{10} cm, the diffusion time is of the order of 10^6 s); hence it is justified to assume that the stream behaves adiabatically.

In the case where the spin of the secondary is aligned and synchronous with the orbit, we can determine the density distribution in the neighbourhood of the L_1 point by expanding the potential around this point in a Taylor series (see e.g. Lubow & Shu 1975, hereafter LS), where we use Cartesian coordinates (x, y, z):

$$\Phi = \Phi_{L1} - (2A+1)\frac{(x-x_{L1})^2}{2}\Omega^2 + (A-1)\frac{y^2}{2}\Omega^2 + A\frac{z^2}{2}\Omega^2, \tag{5}$$

where A is the positive dimensionless constant for a given binary:

$$A = \frac{\mu}{|x_{L1}/D - 1 + \mu|^3} + \frac{1-\mu}{|x_{L1}/D - \mu|^3}. \tag{6}$$

Here Ω is the angular speed of the binary and $\mu = M_1/(M_1+M_2)$.

As the flow of the stream is adiabatic to good approximation, the Bernoulli integral is a conserved quantity in the stream:

$$B \equiv \Phi + \frac{u^2}{2} + \frac{c^2}{\gamma - 1} = \Phi_{L_1} + \frac{u_{L_1}^2}{2} + \frac{c_{L_1}^2}{\gamma - 1}. \tag{7}$$

Here u_{L_1} and c_{L_1} are the velocity and the sound speed of the matter at L_1, and γ is the adiabatic index of the stream material. We assume that in the L_1 neighbourhood the stream is laterally in hydrostatic equilibrium. This is a good approximation, especially in the z-direction (LS). Using equation (5) with $x = x_{L1}$, we can write the potential in the yz-plane as

$$\Phi - \Phi_{L1} = \left(\frac{A-1}{2}y^2 + \frac{A}{2}z^2\right)\Omega^2 \approx \frac{\alpha}{2}r^2\Omega^2, \tag{8}$$

where r is the distance to the L_1 point and $\alpha \approx A$ is a dimensionless constant which depends on the shape of the potential in the neighbourhood of L_1. For binary systems with a mass ratio, q, between 0.006 and 1.0, it has a value of 6.16 to 8.0 (LS). Then the density distribution within an adiabatic stream can be obtained from the condition of lateral hydrostatic equilibrium and from equation (8) as

$$\rho = \rho_c \left(1 - \frac{\alpha}{2}\frac{r^2}{\widetilde{W}^2}\right)^{1/(\gamma-1)} \tag{9}$$

where ρ_c is the density of the material in the core of the stream, and $\widetilde{W}$ is the characteristic width of the stream, which depends on the properties (e.g. entropy, temperature) of the matter in the secondary:

$$\widetilde{W} = \sqrt{\frac{\gamma}{\gamma-1}}\frac{s^{1/2}\rho_c^{1/3}}{\Omega}. \tag{10}$$

Here $s = P/\rho^\gamma$ is the adiabatic constant of the material from the secondary. An adiabatic stream cannot have a width wider than $W = \widetilde{W}\sqrt{2/\alpha}$ (as can be seen directly from equation 9).

We assume that the velocity of the material at L_1 is given by the local sound speed (see LS) and that this speed varies through the stream cross-section. Then, integrating the mass-flow rate across the stream cross-section near L_1, we can relate the mass-loss rate $\dot{M}_2$ (in units of $M_\odot$ yr^{-1}) to the density in the stream core for an adiabatic stream (with $\gamma = 5/3$):

$$\rho_c = 1.4\times10^{-3}\ \mathrm{g\ cm^{-3}}\,\dot{M}_2^{1/2}\Omega_4 s_{15}^{-3/4}\left(x_s^2 - \frac{\alpha}{2}x_s^4 + \frac{\alpha^2}{12}x_s^6\right)^{-\frac{1}{2}}, \tag{11}$$

where $s_{15} = (P/\rho^\gamma)/(10^{15}$ cgs) is the scaled adiabatic constant of the material from the secondary, $\Omega_4 = \Omega/10^{-4}$ s^{-1}, $x_s = W/\widetilde{W}$ is the dimensionless stream width.

Using equation (11) and assuming that the stream has maximum width, i.e. $x_s = \sqrt{2/\alpha}$, it is easy to show that, for a mass-loss rate of order 1 $M_\odot$ yr^{-1}, the pressure at the centre of the stream does not exceed $\sim10^{10}$ dyn cm^{-2}. This value is generally lower than the pressure found in the hot, high-pressure environment of a common envelope, where the pressure is typically in the range of 10^{10}–10^{12} dyn cm^{-2}. This implies that the stream will generally be compressed by the pressure in the ambient envelope. We can estimate its initial width by assuming that the outer edge of the stream is in pressure balance with the common envelope (CE). The stream density at the edge cannot be less than

$$\rho_{\mathrm{out}} = (P_{\mathrm{CE}}/s)^{1/\gamma},$$

where P_{CE} is the ambient pressure in the common envelope. The stream width for the current mass loss rate can then be found from equation (11) in combination with

$$\rho_c = (P_{\mathrm{CE}}/s)^{1/\gamma}\left(1 - \frac{\alpha}{2}x_s^2\right)^{-1/(\gamma-1)} \tag{12}$$

(from equation 9).

2.3 The effect of non-synchronous rotation

Because the spin of the secondary may not be synchronous with the orbit (in fact, it may be rotating faster or more slowly depending on the circumstances), we also need to consider the case of non-synchronous rotation. For this purpose we adopt a coordinate system that rotates with the secondary. At the equipotential surface which determines the surface of the secondary (the donor), there is an area where matter is being accelerated outwards from the stellar surface. From this zone matter may flow out. In the case of a synchronized secondary, the physical situation is a close analogue of a Laval nozzle, where the equipotential surfaces take over the role of a nozzle. In the standard case, when a thin flow is considered, L_1 can be taken as a point. Then, as for the case of the standard Laval nozzle, matter is almost completely unaffected by external acceleration at the nozzle mouth (at the sonic point), but experiences negative acceleration before and positive acceleration after passing though the nozzle.

For an asynchronously rotating secondary, the position of the positive acceleration zone with respect to the secondary changes with time. To parametrize the degree of asynchronicity, we introduce a parameter f,

$$f = \frac{\Omega_{\mathrm{sec}}}{\Omega} - 1, \tag{13}$$

where Ω_{sec} is the angular velocity of the secondary. The parameter f is zero if the secondary rotates synchronously. The position of the point where the acceleration experienced by matter on the stellar surface becomes non-negative can be found similarly to the L_1 point (in order to avoid confusion with the standard L_1 point, we refer to this point as the 'leaving point', LP), considering the generalized Roche potential, Ψ, for the frame with the origin at the centre of the secondary, which rotates with the secondary (see e.g. Limber 1963; Kruszewski 1963):

$$\Psi = \Phi - \frac{\zeta^2+\eta^2}{2}f(f+2)\Omega^2. \tag{14}$$

Here Φ is the usual potential of the binary

$$\Phi = -\frac{GM_1}{|\boldsymbol{r}_1|} - \frac{GM_2}{|\boldsymbol{r}_1|} - \frac{1}{2}(\Omega\boldsymbol{e}_z\times\boldsymbol{r})^2 \tag{15}$$

and (ζ, η) are Cartesian coordinates in the frame rotating with the secondary. For a secondary which rotates faster than the binary itself, LP will normally be shifted from L_1 towards the donor; and, for a secondary which rotates more slowly than the binary, this point will be shifted towards the primary. A rough estimate of the linear speed with which the zone of positive acceleration travels across the secondary surface, $v_{\mathrm{zone}} = f\Omega_{\mathrm{sec}}r_{\mathrm{sec}}$, shows that it is typically twice the local sound speed of the secondary (for the case of $f = 1$ and considering parameters characteristic for a system at the point where the secondary starts to overfill its Roche lobe). In this case, we do not have a normal nozzle (as for a synchronized secondary), as matter at a particular position on the surface of the secondary (in the frame rotating with the secondary) is not affected by any matter that has escaped from the secondary before it enters the zone of non-negative acceleration. Therefore we may consider what happens to a fluid element on the secondary independently from any matter that has flowed out previously. A physical analogue of this situation is a ball, containing the (secondary) matter, that is separated from the outside by negative acceleration. At the surface of the ball there is a hole which travels with supersonic speed. As far as the matter in the ball is concerned, the surface of the ball acts like a wall that is suddenly being removed (for some period of time) and then put back again. Matter will escape from the ball through the hole only if the duration of the interval of positive acceleration is long enough for matter to be able to escape before it is pulled back by the negative acceleration. Another analogue of the problem is the sudden expansion of a gas sphere into vacuum. In this case, the speed with which matter expands can be as high as 3 times the sonic speed (see e.g. Zeldovich & Raizer 1966). In a real situation, we may expect a combination of these and other effects that cannot be easily treated analytically. As this discussion shows, for an asynchronously

rotating secondary, the range of the possible initial flow velocities includes significantly supersonic speeds. Fortunately, our ballistic calculations in Section 3 show that the stream properties close to the primary core are not strongly dependent on the initial flow velocity in the stream.

2.4 The escape angle – generalization of the LS formalism

In the case where the spin of the secondary is not synchronous with the orbit, the angle at which matter leaves the secondary will be different from the synchronous case analysed by LS. To obtain this angle in our problem, we generally follow the LS formalism with the following changes: we place the origin of the coordinate system not at L_1 but at LP, and we use a coordinate frame which rotates with the secondary. Using cylindrical coordinates, the potential (14) in the neighbourhood of LP can be expanded in a Taylor series around LP (in the $Z = 0$ plane) as

$$\Phi = \Phi_{LP} - \left[1 + f(f+2) + \frac{A_{LP}}{2}(3\cos 2\theta + 1)\right]\frac{r^2}{2}\Omega^2, \qquad (16)$$

where A_{LP} is the positive dimensionless constant for a binary with an asynchronously rotating secondary:

$$A_{LP} = \frac{\mu}{|x_{LP}/D - 1 + \mu|^3} + \frac{1-\mu}{|x_{LP}/D + \mu|^3}, \qquad (17)$$

where x_{LP} is the distance between the centre of mass and LP, and θ is the angle between the flow direction of the stream and the direction of the primary.

Similar to the derivation in LS, we use this expansion of the potential in the neighbourhood of LP in the hydrodynamical equations (analogously to equations 14a–c in LS) and obtain a system of equations for the modified radial velocity, $U(\theta_s) = (u_r/c)(D/r)$, and the escape angle θ_s (analogously to equations 23a and b in LS):

$$U^2(\theta_s) = 1 + \frac{A_{LP}}{2}(3\cos 2\theta_s + 1) + f(f+2),$$
$$U(\theta_s) = -\frac{3}{4}A_{LP}\sin 2\theta_s \qquad (18)$$

After the elimination of $U(\theta_s)$, the escape angle of the stream in the frame rotating with the secondary can be found from the equation

$$\cos^2 2\theta_s + \frac{8}{3}\cos 2\theta_s + \frac{16}{9A_{LP}^2}\left[\frac{A_{LP}}{2} + 1 + f(f+2) - \frac{9A_{LP}^2}{16}\right] = 0. \qquad (19)$$

For the case of a synchronously rotating secondary ($f = 0$), this equation reduces to the solution for θ_s obtained by LS. The angle with which the stream will escape from LP in the frame co-rotating with the binary is given by the transformation

$$\tan\theta = \frac{f\Omega D(1 - \mu + x_{LP}/D) + v_e \sin\theta_s}{v_e \cos\theta_s}, \qquad (20)$$

where v_e is the velocity of the stream at the nozzle (sonic for a synchronously rotating secondary).

3 THE BALLISTIC PHASE

The motion of the stream can be naturally divided into two phases, a (quasi-)ballistic phase where the stream trajectory is not strongly affected by the interaction with the ambient matter, which can be treated more or less ballistically, and a hydrodynamical phase where the dynamics of the stream is dominated by the hydrodynamical interaction with the core. Considering these two phases separately helps to avoid numerical problems (due to the complexities near the L_1 point) at the start of the hydrodynamical calculation. However, it also introduces some uncertainty, because matter in the inner region surrounding the primary core may not be in complete co-rotation with the orbit and may have a backward motion with respect to the co-rotating frame. Such relative rotation causes a force which reduces the interception angle between the falling stream and the normal direction to the core relative to the predictions from a purely ballistic trajectory.

The equations for the trajectory of a steady stream in the frame rotating with the binary are

$$u_x\frac{\partial u_x}{\partial x} + u_y\frac{\partial u_x}{\partial y} = -\frac{\partial\Phi}{\partial x} + 2u_y\Omega - \frac{1}{\rho}\frac{\partial P}{\partial l}\frac{u_x}{u},$$
$$u_x\frac{\partial u_y}{\partial x} + u_y\frac{\partial u_y}{\partial y} = -\frac{\partial\Phi}{\partial y} - 2u_x\Omega - \frac{1}{\rho}\frac{\partial P}{\partial l}\frac{u_y}{u}. \qquad (21)$$

Here $u = \sqrt{u_x^2 + u_y^2}$ is the magnitude of the central stream velocity, and u_x, u_y are its components. In these equations we included the pressure gradient along the path $(1/\rho)\,\partial P/\partial l$ (see the derivation of standard equations describing a ballistic trajectory e.g. in LS). This term is generally small since the Mach number of the flow is large except near the nozzle. It is kept here for completeness and consistency in the calculations. The structure of the common envelope enters into these equations through the pressure boundary condition at the stream edge, which is set equal to the ambient pressure in the envelope. The density within the stream is related to the pressure by the adiabatic constant of the secondary material $s = P/\rho^\gamma$ = constant. Together with a specified mass-flow rate, these equations provide a complete set of equations that fully describe the dynamics of the stream in this phase.

3.1 Initial conditions for the hydrodynamical calculations

The initial conditions for the hydrodynamical simulations are taken directly from the parameters obtained from the ballistic calculations for a range of binary parameters. Specifically, we consider parameters representing the spiral-in and subsequent merger of a secondary of 1 and 5 $M_\odot$ inside a 20-$M_\odot$ evolved supergiant which has completed helium burning in the core and has a core mass of $\sim$7 $M_\odot$. To model the secondaries, we first followed their evolution to the same age as the primary and then evolved them further, subjecting them to very rapid mass loss in order to model their adiabatic response to it. These calculations give the radii of the stars and their surface entropies as a function of current stellar mass.

Tables 1 and 2 (upper parts) illustrate the evolution of the stream properties during the ballistic phase as the secondary mass decreases. Here, the initial parameters for the ballistic calculations, such as the entropy and separation, were determined from the current mass of the secondary (note that these calculations did not take into account any changes in the properties of the core and the surrounding envelope during the merging phase; these will be treated self-consistently in IP). The mass-flow rate does not strongly affect the results apart from the stream width. In the bottom parts of Tables 1 and 2 we present the results of calculations for the same CE systems, but where we set the asynchronicity parameter to $f = 1$ (i.e. where the secondary rotates twice as fast as the binary).

4 THE NUMERICAL METHOD

4.1 The hydrodynamics code

For the hydrodynamical simulations of the stream–core interactions we use a code based on the PROMETHEUS hydrodynamical code

Table 1. Stream properties at the end of the ballistic calculation representative for a $20 + 1$ $M_\odot$ CE simulation, at the top part of the table – the synchronously rotating secondary, at the bottom – the secondary rotates with twice the orbital angular velocity.

M_2	$\log s$	D [10^{11} cm]	$M_{\rm int}$	$M_{\rm ext}$	$v_{\rm fin}$[10^8 cm s^{-1}]	η_ρ	Θ	$R_{\rm str}[\pi]$
1.0	14.88	2.6	5.6/5.0	1.8/2.1	0.73/1.02	11.3/6.9	41°/47°	0.024/0.014
0.8	14.70	2.2	5.2/5.1	1.5/1.9	0.60/0.93	14.6/8.8	39°/45°	0.023/0.013
0.6	14.32	2.1	6.6/6.7	1.4/1.9	0.58/0.93	24.8/15.0	39°/46°	0.018/0.010
0.4	14.14	2.3	9.3/8.5	1.8/2.1	0.73/1.05	31.5/19.1	47°/56°	0.014/0.008
1.0	14.88	2.6	5.0/4.5	1.8/2.0	0.73/1.01	15.7/9.2	45°/51°	0.020/0.012
0.8	14.70	2.2	4.7/4.6	1.5/1.9	0.60/0.92	19.6/11.6	44°/50°	0.020/0.011
0.6	14.32	2.1	6.1/6.1	1.5/1.9	0.59/0.92	32.1/19.0	48°/54°	0.016/0.009
0.4	14.14	2.3	8.7/7.9	1.8/2.1	0.74/1.04	39.7/23.7	53°/63°	0.013/0.007

Notes. M_2: mass of the secondary, the mass donor. $\log s$: logarithm of the adiabatic constant (p/ρ^γ in cgs units). D: binary separation. In all cases, the initial stream velocity was assumed to be the local sound speed. Stream parameters (at two different radii from the primary core, 10^{11} and 7.5×10^{10} cm, respectively). $M_{\rm int}$, $M_{\rm ext}$: internal and external Mach numbers of the stream material (i.e. relative to the stream sonic velocity and relative to the ambient sonic velocity). $v_{\rm fin}$: stream velocity. η_ρ: ratio of the central stream density to the ambient density. Θ: stream angle relative to the primary core centre. $R_{\rm str}$: angular radius of the stream. The values are representative for CE systems consisting initially of a giant of 20 $M_\odot$ (with a 7 $M_\odot$ core) and a 1 $M_\odot$ secondary, where the secondary is assumed to lose mass at a rate of $\dot{M} = 1$ $M_\odot$ yr^{-1}. The ambient temperatures and densities at the radii given in the table are ($T = 6 \times 10^6$ K, $\rho = 5 \times 10^{-3}$ g cm^{-3}) and ($T = 10^7$ K, $\rho = 2.5 \times 10^{-2}$ g cm^{-3}), respectively.

Table 2. Stream properties at the end of the ballistic calculation representing a $20 + 5$ $M_\odot$ CE simulation, at the top part of the table – the synchronously rotating secondary, at the bottom – the secondary rotates with twice the orbital angular velocity.

M_2	$\log s$	D [10^{11} cm]	$M_{\rm int}$	$M_{\rm ext}$	$v_{\rm fin}$[10^8 cm s^{-1}]	η_ρ	θ	$R_{\rm str}[\pi]$
5.0	16.50	5.1	1.3/0.8	1.4/1.1	0.64/0.53	1.1/0.6	29°/15°	0.098/0.076
4.0	15.05	3.4	5.1/4.8	1.6/2.1	0.74/1.03	11.8/6.4	33°/36°	0.027/0.017
3.0	14.90	3.4	6.1/5.6	1.8/2.2	0.80/1.08	14.5/7.7	35°/40°	0.023/0.015
2.0	14.85	3.7	7.0/6.2	2.0/2.3	0.89/1.16	15.6/8.4	41°/46°	0.021/0.014
5.0	16.50	5.1	1.0/0.6	1.1/0.9	0.50/0.45	1.5/0.9	17°/7°	0.093/0.069
4.0	15.05	3.4	4.6/4.3	1.6/2.1	0.74/1.02	15.7/8.5	45°/47°	0.023/0.015
3.0	14.90	3.4	5.6/5.0	1.8/2.2	0.80/1.08	19.2/10.4	21°/25°	0.020/0.013
2.0	14.85	3.7	6.5/5.7	2.0/2.3	0.89/1.15	19.7/10.7	53°/60°	0.019/0.012

Notes. Similar simulations as those in Table 1 for a CE systems consisting initially of a 20-$M_\odot$ giant (as before) and a 5-$M_\odot$ secondary. The stream parameters are given at radii of 10^{11} and 7.5×10^{10} cm, respectively. The ambient temperatures and densities at these radii are ($T = 7 \times 10^6$ K, $\rho = 7 \times 10^{-3}$ g cm^{-3}) and ($T = 10^7$ K, $\rho = 3 \times 10^{-2}$ g cm^{-3}), respectively.

(Fryxell, Müller & Arnett 1989). This is an Eulerian code, which uses a second-order Godunov-type scheme to solve the hydrodynamical equations, the piecewise parabolic method (PPM) of Colella & Woodward (1984). This code has been widely used by different groups (see e.g. Kercek, Hillebrandt & Truran 1998, hereafter KHT), and we refer to these papers for a detailed description of the code and numerical tests. To make it applicable to our problem, we had to make a number of modifications to the original code, in particular to the treatment of the gravity field, the boundary conditions, to the equation of state and the hydrodynamical equations themselves (to take into account the effects of a frame co-rotating with the binary). Because the mass transfer occurs in an opaque environment, radiative losses are not important and have been neglected.

In the presence of a large pressure gradient at the core-envelope interface and a correspondingly strong gravitational field, Godunov-type schemes produce intrinsic accelerations, which during a few dynamical time-scales $t_{\rm d}$ create significant outward motion (KHT). For a first-order Godunov method, it is possible to find an analytical formula to modify the interface states. Then, source terms (the gravitational field in our case) will be balanced by flux differences (LeVeque 1998). This is not possible for higher-order Godunov-type schemes where each problem requires a separate treatment (KHT). To reduce the artificial acceleration in our case, we assume that the gravitational field can be considered as constant in time and that there is no self-gravity. Then, in each time-step, we modify the interface values before applying the Riemann solver, by reducing them from both (left and right) interfaces by a pressure flux caused by gravity. Furthermore, we enforce the condition of hydrostatic equilibrium at the boundary (for ghost cells[1]) in the direction of the gravity field. These modifications ensure that any initial model remains stable for arbitrarily long time.

4.2 The model set-up

We performed two-dimensional calculations in polar cylindrical coordinates, where we usually used 300×300 grid points. In the case

[1] Ghost cells are a few additional cells (four in the case of a PPMcode) at each boundary of the computational domain, where the values at these cells are determined by the boundary conditions.

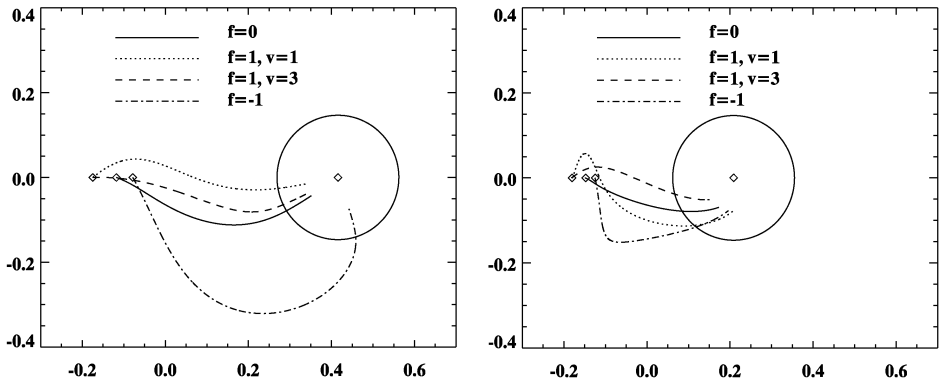

Figure 1. Ballistic trajectories for a stream from a massive secondary (assumed to be on the left-hand side in each panel) falling on to the 7-$M_\odot$ core of a red supergiant inside a common envelope (in dimensionless units). The left-hand panel shows the trajectories at the beginning of mass transfer (when the secondary has a mass of 5 $M_\odot$); the right-hand panel shows the trajectories for the same system at a later stage when the mass of the secondary has been reduced to 3.5 $M_\odot$. The differently labelled trajectories assume different rotation rates for the secondary ($f = 0$: co-rotation with the orbit, $f = 1$: rotating with twice the angular velocity of the binary, $f = -1$: non-rotating). For the case $f = 1$, the trajectories with $v = 1$ and $v = 3$ assume that the initial velocity of the stream material is the local sound speed and 3 times the local sound speed, respectively (in all other cases, the initial speed is taken to be the local sound speed). The large circles indicate a radius of 7.5×10^{10} cm, which we usually choose as the outer boundary for the hydrodynamical calculations.

of very narrow streams, we increased the resolution to 600×600 grid points. We also carried out test calculations with grids of higher resolution to satisfy ourselves that further increasing the number of grid points does not significantly affect the results. As a general rule, we ensure that the inflowing stream contains at least 20 grid points in the azimuthal direction. We also carried out a few three-dimensional calculations (in spherical coordinates) for the case of a symmetrical (non-inclined) stream in a non-rotating frame. The results of these calculations showed that there were no significant differences between the two- and three-dimensional calculations with the same initial parameters. In particular, the penetration depths of the stream were very similar in the corresponding calculations.

4.2.1 *Ambient matter*

To model the structure of the ambient medium in regions where the stream–core interaction occurs inside the common envelope, we adopt power-law distributions for the ambient temperature and pressure, i.e $T(r) = T(r_0)(r_0/r)^{\alpha_T}$ and $P(r) = P(r_0)(r_0/r)^{\alpha_P}$. We fitted these power laws to the structure in actual CE calculations (as described in detail in IP). Typical values for α_T and α_P are in the range (1.3; 5.2)–(0.8; 3.2), but can be as high as (1.7; 7) (corresponding to a structure with an adiabatic index $\gamma_{\rm amb} \approx 1.44$) and reasonably describe the regions of the stellar models at the the evolutionary stage of interest (IP). For our calculations here, we adopted parameters $(\alpha_T; \alpha_P) = (1.3; 5.2)$ and (0.8; 3.2) for models representing a $20 + 1$ and a $20 + 5$ CE simulation, respectively. Throughout the domain of our calculations, we assume that the ambient matter has a constant composition, similar to the composition in the core region of the primary, mainly helium. In the full stellar models, hydrogen is exhausted below a radius of 4×10^{10} cm, and the hydrogen mass fraction increases to ~0.1 at the outer edge of the domain (at 7.5×10^{10} cm). We have tested that these differences do not affect the results appreciably. In this parametrized model, we assume that the ambient matter is initially in (quasi-)hydrostatic equilibrium; as the model is parametrized by the pressure and temperature gradient, the gravitational field is then defined implicitly by the initial pressure gradient of the frame and the initial density distribution. In calculations where nuclear burning is included, we use a nuclear reactions network with 35 isotopes, which includes all important reactions up to ^{25}Mg, in particular all α reactions and the complete hot (β-limited) CNO cycle. The reaction rates were taken from the Thielemann nuclear reactions library (provided by R. C. Cannon). The changes in chemical composition and the energy density due to the nuclear burning are updated after each time-step in the hydrodynamical calculation. To prevent nuclear burning in the ambient medium, we assumed that the ambient medium contained neither H nor He in these particular calculations. (For further details we refer the reader to IP.)

4.2.2 *Boundary conditions*

The boundary conditions in the code, which describe the characteristics of the inflowing stream, are the internal and external Mach numbers, $M_{\rm int}$ and $M_{\rm ext}$; the ratio between the central density in the stream and the ambient density at the outer boundary η_ρ; the initial inclination angle of the stream Θ (i.e. the angle between the initial flow direction and the direction of the primary). For the chemical composition of the gas in the stream we use the abundances of the secondary.

The boundary conditions for the rest of the box in the radial direction are outflow boundaries (except in the gas inflow zone) where the condition of hydrostatic equilibrium has been imposed for ghost cells. The boundary condition in the azimuthal direction also assumes outflow conditions (we used a grid which normally covers an angle π). As the Courant number we used $N_{\rm CFL} = 0.6$–0.8. A further parameter is the angular velocity with which the coordinate system rotates (most calculations were performed in the frame rotating with the primary core).

5 INTERACTION BETWEEN THE STREAM AND THE AMBIENT MATTER

5.1 The initial stream–core interaction: establishing a steady stream

Fig. 2 shows the initial interaction of a stream with a massive core and illustrates the development of a stationary stream. The parameters for this simulation are characteristic for a 1-$M_\odot$ star filling its Roche lobe inside the envelope of a very evolved 20-$M_\odot$ red

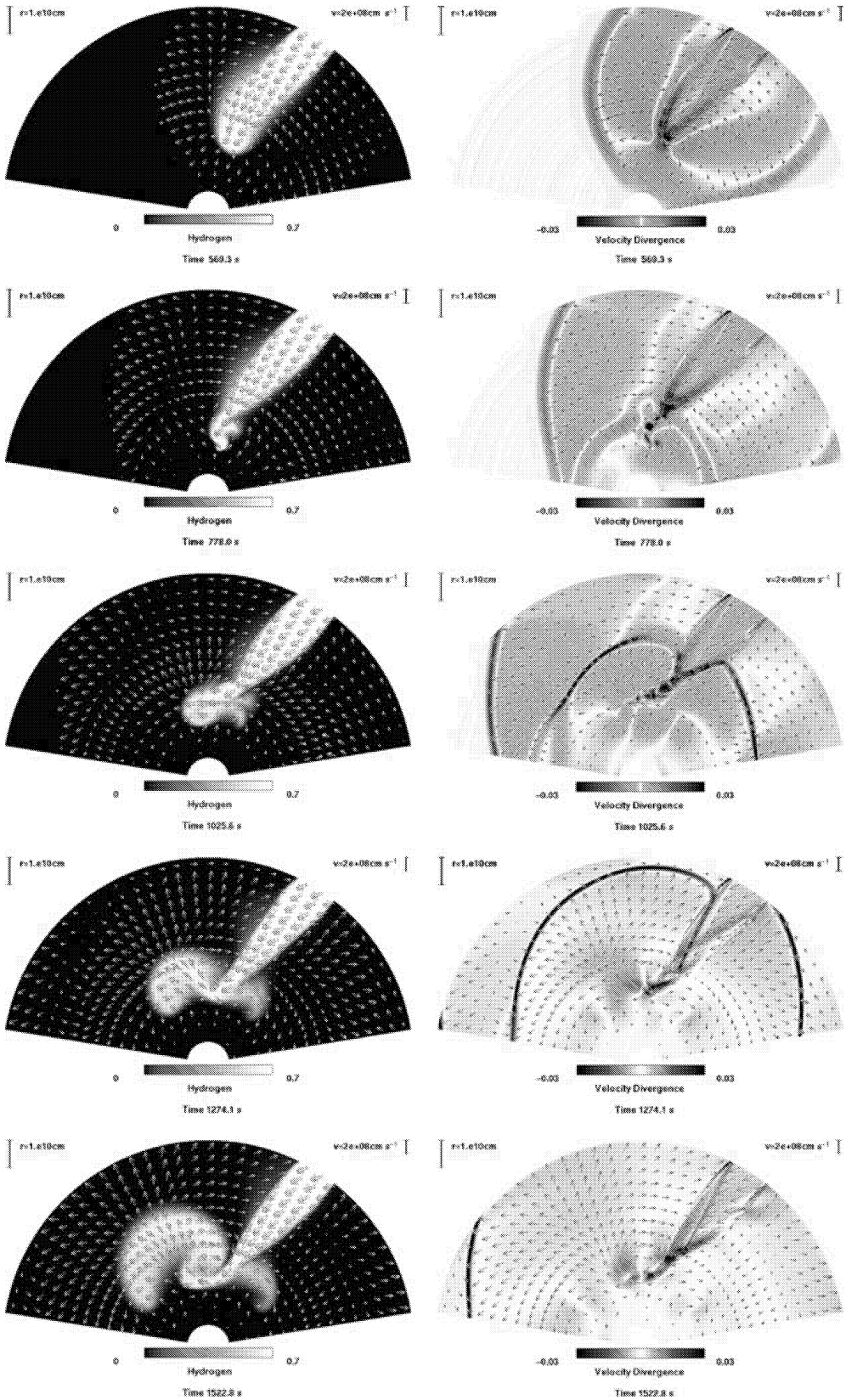

Figure 2. The initial stream–core interaction and the establishment of a steady stream in a frame rotating with the core (with an angular velocity $\Omega_{\rm frame} = 4 \times 10^{-4}$ rad s^{-1}). The left panels show the distribution of hydrogen, the right panels the distribution of $\nabla \cdot \boldsymbol{v}$. The initial Mach numbers in the stream, $M_{\rm int}$, and ambient medium, $M_{\rm ext}$ are 8.5 and 3.2, respectively, the density ratio between the stream and the ambient medium is $\eta_\rho = 8$, the outer radius is $R_{\rm T} = 7.5 \times 10^{10}$ cm, the angular radius of the stream is $R_{\rm s} = 0.03\pi$ and the initial stream inclination with respect to the radial direction is $\Theta = 13.5°$. The velocity field is scaled according to $\log(v/10^6$ cm s$^{-1})$.

supergiant (after helium core burning). The panels on the left show the hydrogen abundance, while the panels on the right show the divergence of the velocity field. The latter was chosen because it shows shock structures particularly clearly.

The top panels show the stream just before its 'impact' with the core (569 s after the beginning of the simulation), while the second set of panels is close to the point of impact (at 778 s; note the bow shock in the right panels). Immediately after the impact, stream matter bounces off the core, where most of it is just reflected by the core and continues to move in the forward direction (i.e. counter-clockwise), but some of it is pushed backwards, attaining an angular velocity component opposite to the rotation of the core. As material that has been stopped by the core is pushed by material in the stream following from behind, it starts to flow up again, driving two powerful shocks on the front and back side of the stream into the envelopes. These shocks compress the stream significantly. Once they have left the domain of the calculation, the stream has attained essentially a stationary configuration, where the point of deepest penetration ($R \simeq 2 \times 10^{10}$ cm) and the stream shape no longer change significantly. The overall flow pattern also becomes more-or-less stationary, where all the matter leaving the stream in the core impact region flows up again, being vigorously mixed with helium from the core in the process.

5.2 Mechanisms for stream dissipation

The main objective of our calculations is to determine how deep the stream can penetrate into the core of a massive star after the initial transient behaviour has passed. In the quasi-stationary situation this depends mainly on the entropy that is generated in the stream–core interaction.

5.2.1 *Pressure discontinuity and entropy generation*

While the stream is in lateral pressure balance with the ambient matter at an early stage of infall, it becomes increasingly unbalanced as the velocity increases and becomes significantly supersonic relative to the ambient medium. The interaction between the stream and the ambient matter due to the jump in pressure can be treated in a simplified way as a Riemann problem (see e.g. LeVeque et al. 1998), a solution of which is a combination of shock and rarefaction waves. In the case where the stream expands, the rarefaction wave, propagating into the stream material, does not change the stream entropy. However, compression of the stream by the ambient matter, in the form of shocks moving into the stream, generates entropy inside the shocks.

For a strong shock, where the ratio of ambient pressure to stream pressure $P_{\rm amb}/P \gg 4$, the coefficient of entropy change, i.e. the ratio of the entropy of the shocked stream material, $S_{\rm s}$, to the initial entropy in the stream, S, can be estimated as

$$K_{\rm S} = \exp[(S_{\rm s} - S)/c_V] = \frac{P_{\rm s}}{P}\left(\frac{\rho_{\rm s}}{\rho}\right)^{\gamma} \approx \text{constant} \times P_{\rm amb}/P \quad (22)$$

(Zeldovich & Raizer 1966).

In our case, we rather expect the development of weak shocks. Then an estimate for $K_{\rm S}$ can be written as

$$K_{\rm S} \approx 1 + \text{constant} \times \eta_{\rho}^{\gamma-1}\left(\frac{M_{\rm int}}{M_{\rm ext}}\right)^2 (P_{\rm amb}/P - 1)^3 \quad (23)$$

(Zeldovich & Raizer 1966). The pressure jump $P_{\rm amb}/P$ changes with the distance to the primary core. In the case of a power-law parametrization of the ambient pressure, equation (23) predicts that models with smaller power-law indices will result in smaller pressure jumps for the same initial stream properties and hence smaller values for $K_{\rm S}$, and that this coefficient increases as the power-law index increases.

In Fig. 3 we present some of the key characteristics of a stream with the same parameters as in Fig. 2, once a more-or-less stationary flow pattern has been established. Note in the top two panels that the entropy in the core of the stream is initially constant and that all the entropy generation takes places in two strong shocks at the stream boundaries (clearly seen in the $\nabla \cdot \boldsymbol{v}$ panel). All of the stream matter has to pass through the intersection of these shock structures, where it essentially attains its final entropy and where the adiabatic constant of the stream material becomes comparable to the adiabatic constant of the ambient material. For the entropy the difference between ambient and stream matter is largely caused by the difference in molecular weights and its subsequent change is due to mixing of these two media rather than dissipation. At the point of deepest penetration ($\sim 2 \times 10^{10}$ cm), the stream matter has a temperature of 6×10^7 K and a density of ~ 3 g cm^{-3}, high enough for nuclear burning (see Section 5.4).

5.2.2 *Kelvin–Helmholtz instabilities and the stream width*

The Kelvin–Helmholtz (K–H) instability affects both the stream shape and the stream width. For small relative velocities, the stream is 'sausage-shaped' and becomes increasingly 'snake-shaped' as the relative velocity increases (see Fig. 4). It becomes more important as the stream narrows, since perturbations of a given wavelength are more important for a narrower flow. It therefore determines the minimum stream width and thus limits the depth of penetration. In particular, a stream that is very narrow initially will penetrate less deeply than a stream with otherwise similar parameters (e.g. velocity, density and pressure), but with a larger mass-flow rate and hence larger initial stream width.

5.3 The effects of rotation

5.3.1 *A rotating medium*

In some cases, in particular near the end of the merging process, the envelope surrounding the spiraling-in components may no longer remain in co-rotation with the binary (either because the spiral-in time-scale becomes too short or because the region surrounding the primary core expands rapidly). Then the stream feels an additional force due to the moving external medium. This affects the trajectory of the stream, in particular the angle of incidence, and thereby the penetration depth. This is illustrated in Fig. 5 which shows two stream calculations with the same parameters as in Fig. 3 but where the medium is assumed to rotate with an angular velocity $\Omega_{\rm shift} = 10^{-4}$ rad s^{-1} relative to the frame of the binary (rotating with angular velocity Ω) either in the forward or in the backward direction. The frame of the medium (in which the calculation is performed) then rotates with a velocity $\Omega_{\rm amb} = \Omega \pm \Omega_{\rm shift}$. In this frame, the stream itself rotates either anti-clockwise (left-hand panel) or clockwise (right-hand panel). As the stream is being pushed backwards by ambient matter moving against its direction of rotation, its trajectory steepens and consequently the penetration depth increases (left panel), while the opposite happens when the stream is pushed from behind (right panel). As a consequence the stream penetrates deeper to a radius of $\sim 1.75 \times 10^{10}$ cm instead of $\sim 2 \times 10^{10}$ cm in

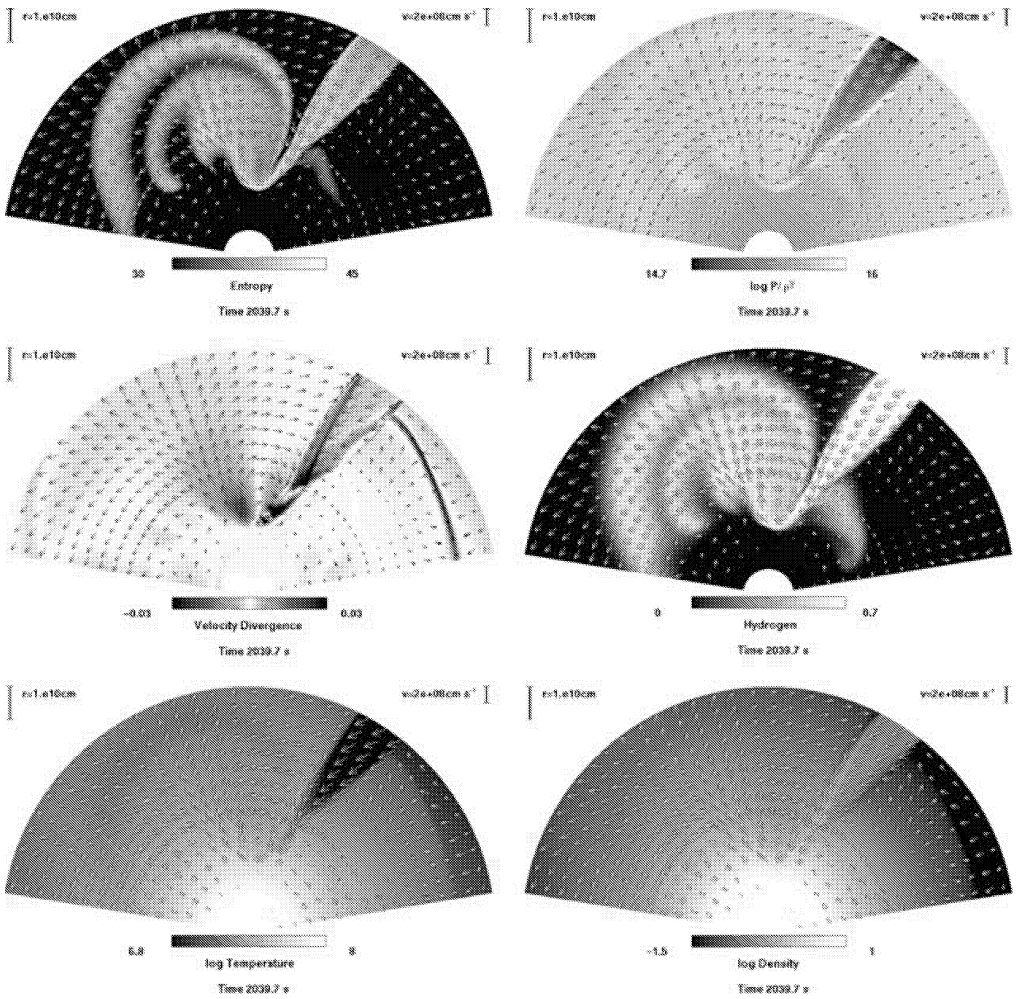

Figure 3. Characteristic properties (entropy, log P/ρ^{γ}, divergence of velocity, hydrogen mass fraction, density and temperature) for a stationary inclined stream (with the same parameters as in Fig. 2). The radius of deepest penetration is 2.0×10^{10} cm in the simulation. At that depth the temperature in the stream is 6×10^{7} K and the density 3 g cm^{-1}.

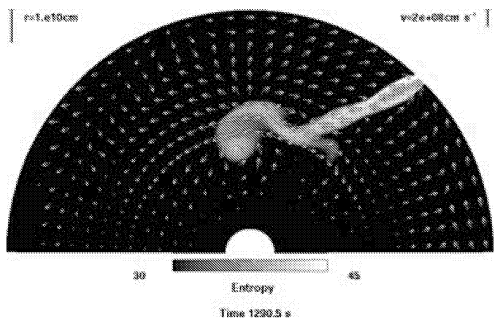

Figure 4. Example of a Kelvin–Helmholtz instability experienced by a narrow stream with $R_{\rm s} = 0.005\pi$ ($M_{\rm int} = 8$, $M_{\rm ext} = 3.25$, $\eta_{\rho} = 8$, $R_{\rm T} = 7.5 \times 10^{10}$ cm, $\Omega_{\rm frame} = 4 \times 10^{-4}$ rad s^{-1}, $\Theta = 18°$). The stream penetrates to a depth of 2.7×10^{10} cm.

the standard case (Fig. 3), while it only reaches a depth of $\sim 2.25 \times 10^{10}$ cm in the opposite case. The corresponding change in the stream temperature at the deepest point is only a few per cent. Note also that for the stream rotating anti-clockwise, the entropy generation at the back side of the stream, where the dynamical pressure is smaller than at the front side (and hence has a larger jump in pressure), is larger than for a stationary inclined stream.

5.3.2 *Core rotation*

As the stream interacts with the core, it injects not only matter but also angular momentum into the core, spinning it up in the process. As the core only has to accrete a small fraction of the angular momentum available from the secondary to be spun up to critical rotation, we may expect that this itself will affect the dynamics of the interaction. To demonstrate this, we performed four simulations for streams with the same initial parameters and similar core properties except that we varied the rotation of the core from 0 to 0.005 rad s^{-1} within a core radius of 4×10^{10} cm. [2] The results of these simulations are shown in Figs 6 and 7.

As Fig. 6 shows, the core–stream interaction changes qualitatively and quantitatively, where the penetration depth decreases

[2] Note that these cores are not completely comparable, as we assumed that the ambient core matter was in quasi-static dynamical equilibrium and had the same pressure and temperature distributions in all cases. This implies slightly different gravitational accelerations (and hence different core masses).

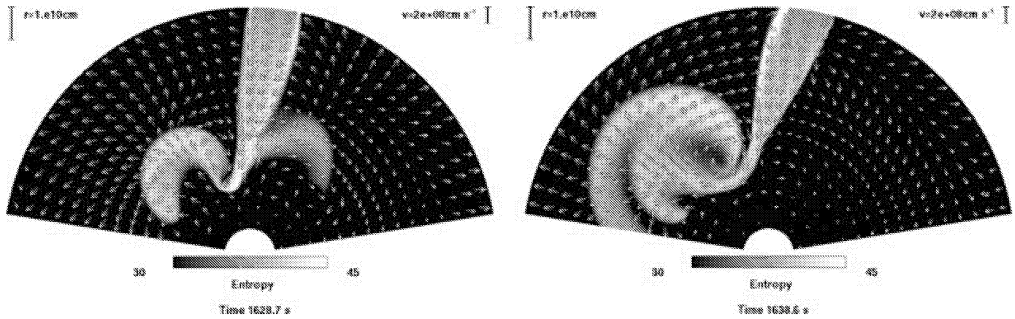

Figure 5. Examples for streams penetrating into a medium rotating relative to the binary. The stream rotates in an anti-clockwise and a clockwise direction relative to the medium in the left- and right-hand panels, respectively, with a relative velocity $\Omega_{\rm shift} = 10^{-4}$ rad s^{-1}. The initial positions of the stream centre in the azimuthal direction were taken to be 0.3π and 0.6π in the two cases, respectively. The other stream parameters are the same as in Fig. 3 ($M_{\rm int} = 8.5$, $M_{\rm ext} = 3.2$, $\eta_\rho = 8$, $R_{\rm T} = 7.5 \times 10^{10}$ cm, $R_{\rm s} = 0.03\pi$, $\Omega_{\rm amb} = 4 \times 10^{-4}$ rad s^{-1}, $\Theta = 13.5°$). The radii at the point of deepest penetration are 1.75 and 2.25×10^{10} cm, respectively.

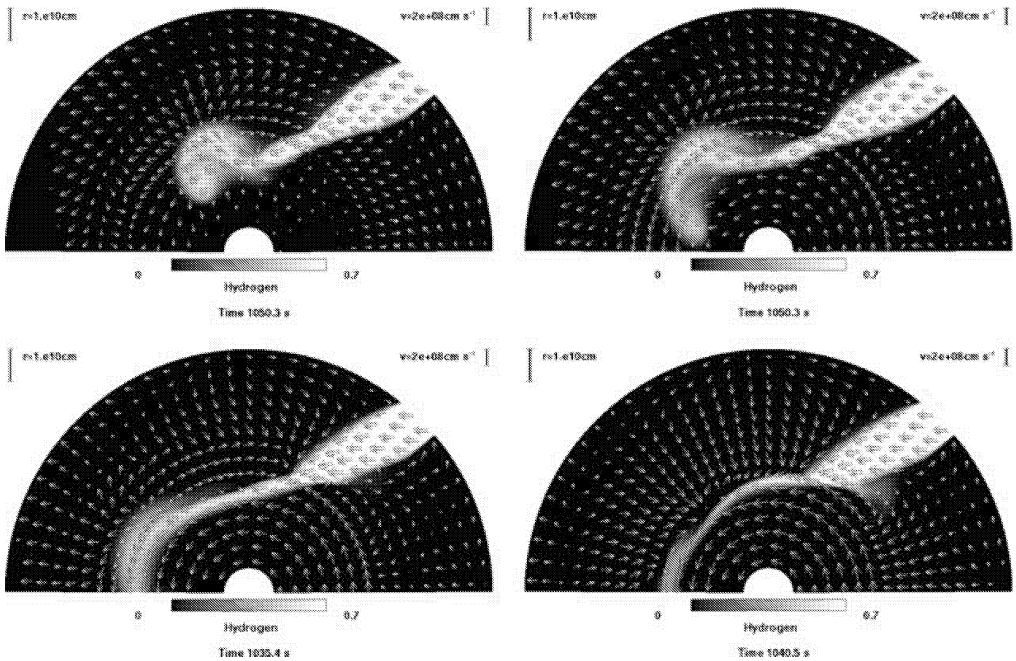

Figure 6. Stream simulations illustrating the effects of rotation of the primary core (in a frame rotating with the binary). In the four calculations, the core is assumed to rotate with constant angular velocities of $\Omega_{\rm core} = 0$ (top left), 0.001 (top right), 0.0025 (bottom left) and 0.005 rad s^{-1} (bottom right), respectively, up to a radius 4×10^{10} cm. The other stream parameters are $M_{\rm int} = 9.8$, $M_{\rm ext} = 3.7$, $\eta_\rho = 8.4$, $R_{\rm T} = 7.5 \times 10^{10}$ cm, $R_{\rm s} = 0.025\pi$ and $\Theta = 18°$.

with increasing core rotation. In the case of a rapidly rotating core, the penetration depth is centrifugally limited (i.e. by the angular momentum in the stream). In Fig. 7 we show the logarithm of the adiabatic constant and the specific angular momentum near the centre of the streams in the four simulations as a function of radius. In the two simulations with no or slow core rotation (solid and dashed curves), the angular velocity of the stream is efficiently braked below a radius 2.6×10^{10} cm by its interaction with the core, and reaches the deepest point of penetration (marked as filled circles) where the adiabatic constant is comparable to the ambient one. The specific angular momentum is always substantially less than the local critical angular momentum for centrifugal support, given by $\sqrt{gR^3}$, where g is the gravitational acceleration at radius R. On the other hand, in the two cases with rapid core rotation (dot-dashed and triple-dot-dashed curves), the stream is first accelerated in the azimuthal direction by the interaction with the core, in fact reaching an angular velocity that is larger than the local velocity of the core (even though the initial angular velocity at the core boundary was smaller). At the point of deepest penetration, the specific angular momentum is close to the critical angular momentum, and hence the stream becomes centrifugally supported. Note also that, in this case, the stream does not bounce but starts to form a ring that orbits the core and gradually mixes with it. This demonstrates that the main effect of rapid core rotation is to *prevent/reduce* the azimuthal braking of the stream. While this leads to less entropy generation in the stream (see the top panel in Fig. 7), which ordinarily would mean that the stream should be able to penetrate deeper, it also makes the angular momentum of the stream itself a key factor in limiting the penetration depth. In the simulation with the fastest core, the stream matter is still substantially denser than the ambient matter at the final point shown in the simulations. As it is also rotating faster than the local core material, it is reasonable to expect that the stream will continue to spiral in as it is being braked by the ambient medium and will penetrate somewhat deeper than is shown in the figures. (We

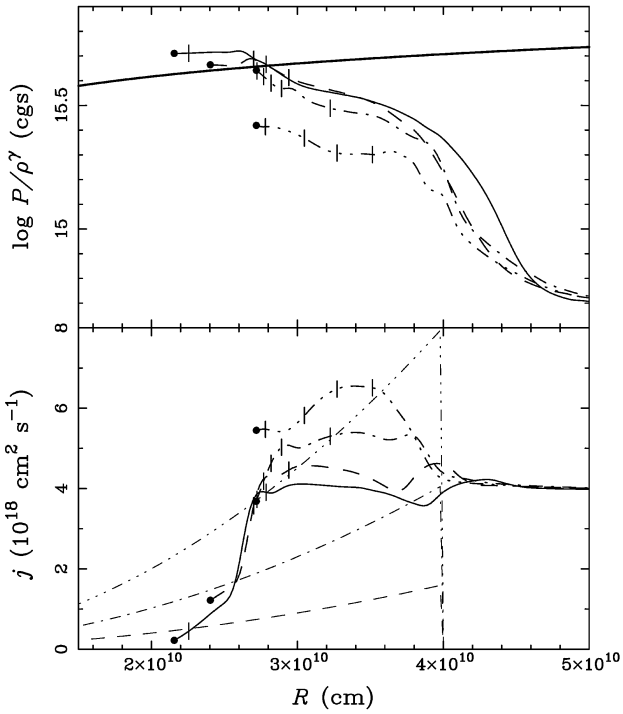

Figure 7. The logarithm of the adiabatic constant ($s = P/\rho^\gamma$, top panel) and specific angular momentum (bottom panel) near the centre of the streams as a function of penetration depth for the simulations in Fig. 6 with angular velocities $\Omega = 0$ (solid curves), 0.001 (dashed curves), 0.0025 (dot-dashed curves) and 0.005 rad s^{-1} (triple-dot-dashed curves). The corresponding angular-velocity profiles for the ambient core matter are shown in the bottom panel as lighter curves with the same line style. The thick solid curve in the top panel refers to log s in the ambient matter. The filled circles at the end of individual curves mark the points of deepest penetration. The ticks along each curve indicate particular values of the central stream hydrogen abundance by mass (0.6, 0.5, 0.4, 0.3 from right to left).

were unable to follow the subsequent evolution because the stream matter was leaving the domain of the calculation at this point.)

Even in the case where the core is non-rotating, the specific angular momentum in the stream increases during a portion of its trajectory (see the solid curve in the bottom panel between 3 and 3.8×10^{10} cm). This is a direct consequence of the stream splitting into two components in the impact region, a forward and a backward component (this can be seen more clearly in Figs 1 and 2). As matter in the forward component is pushed by matter following from behind, it is being accelerated and gains angular momentum, while matter flowing backwards attains negative angular momentum.

Finally, note that because of the narrower stream in the post-impact region of the more rapidly rotating core, stream material mixes more efficiently with the core material (Figs 6 and 7). This may have important consequences for the nucleosynthesis in this region (see Section 5.5 and IP).

5.4 The inclination angle and the penetration depth

The penetration depth also depends on the inclination angle of the stream, which in turn is determined by the initial stream angular momentum and the ballistic trajectory of the stream before its impact with the core (see Fig. 1). To investigate this dependence, we performed a set of simulations for streams with parameters $M_{\rm int} = 5.6$, $M_{\rm ext} = 2.2$, $\eta_\rho = 8$, $R_{\rm T} = 7.5 \times 10^{10}$ cm, $R_{\rm s} = 0.03\pi$, where we varied the initial inclination angle systematically: $\Theta = 9°$, 18°, 27°, 36°, 45°, 54°, respectively. In the first two cases, the initial specific angular momentum, j_0, is smaller than the local critical angular momentum $j_{\rm c}$, for which a stream could be centrifugally supported, for most of the domain of the calculation, while in the other cases j_0 becomes larger than j_c at radii $r_{\rm centr} = 1.2 \times 10^{10}$, 2.6×10^{10}, 4.1×10^{10}, 6.0×10^{10} cm, respectively.

As soon as the stream starts to interact strongly with the core, it also begins to mix with core material. Hence, as the stream penetrates deeper, its hydrogen mass fraction decreases. In Table 3 we present the depth of deepest penetrations in these simulations for stream material with different hydrogen mass fractions ($X = 0.2, 0.4, 0.5, 0.6$), once a steady-state stream has been established. In the two cases with the largest inclinations (i.e. $\Theta = 45°$, 54°), a true steady state is never properly established since the mixing process exhibits a burst-like behaviour (see Fig. 8) after the stream has lost most of its specific angular momentum.

The most important result of these simulations is that the streams can efficiently lose their angular momentum once they interact strongly with the core. Fig. 8 shows a typical example for a large initial inclination ($\Theta = 45°$). The stream loses most of its angular momentum by the time it reaches a radius of 4×10^{10} cm. Because it is still denser and has a lower adiabatic constant than the ambient medium, it continues to sink, increasingly mixing with the ambient material. In general, the point of deepest penetration is determined by the condition that the adiabatic constant of the mixed stream material becomes comparable to the ambient adiabatic constant. However, in practice only a small amount of stream material reaches the deepest point (i.e. regions where $X = 0.2, 0.4$). Most of the stream material is mixed with the ambient medium at a larger radius (the detailed behaviour depends strongly on the initial inclination).

Table 3. Dependence of penetration depth on initial inclination angle.

Θ	$X = 0.2$	$X = 0.4$	$X = 0.5$	$X = 0.6$
9	2.0×10^{10}	2.3×10^{10}	2.5×10^{10}	3.2×10^{10}
18	2.0×10^{10}	2.3×10^{10}	2.5×10^{10}	3.3×10^{10}
27	2.5×10^{10}	2.6×10^{10}	2.9×10^{10}	3.5×10^{10}
36	2.5×10^{10}	2.8×10^{10}	3.3×10^{10}	3.7×10^{10}
45	2.7×10^{10}	2.7×10^{10}	3.3×10^{10}	4.2×10^{10}
54	2.8×10^{10}	2.8×10^{10}	3.2×10^{10}	5.0×10^{10}

Note. Θ: initial stream inclination. The different columns show the depth of deepest penetration (in cm) for material in the stream with different hydrogen mass fractions X, as the stream penetrates into the core and mixes with core material.

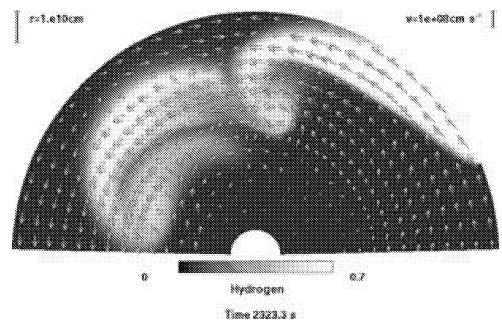

Figure 8. Stream simulation illustrating the effects of a large, initial inclination angle with $\Theta = 45°$. ($M_{\rm int} = 5.6$, $M_{\rm ext} = 2.2$, $\eta_\rho = 8$, $R_{\rm T} = 7.5 \times 10^{10}$ cm, $R_{\rm s} = 0.03\pi$.)

Overall, we can conclude that the dependence on the inclination angle is rather weak and that in general the penetration depth is mainly a function of the stream entropy and the initial velocity, unless the angular momentum in the stream is so large that it becomes centrifugally supported before it can strongly interact with the core.

5.5 The effects of nuclear burning

One of the objectives of our study is to investigate the nucleosynthesis in the stream material after it has been heated by its impact with the core of the primary. The associated heating by nuclear burning itself may then affect the hydrodynamics of the stream. As can already be seen from the simulations presented so far, the characteristic time-scale for the stream infall is of order 1000 s, where the stream material typically spends no more than 50–100 s near the impact region before it bounces or forms a ring orbiting the core (in the case of a fast rotating core). Nuclear burning can only affect the stream motion if the characteristic time-scale for nuclear burning is of order or shorter than the stream dynamical time-scale. For the largest part of the stream trajectory, the stream material is relatively cold (for the range of stream models considered).

Nuclear burning only starts to increase dramatically after it has been heated to a temperature comparable to the ambient temperature, which occurs suddenly in the region of impact. However, because the characteristic nuclear time-scale is generally longer than the local dynamical time-scale, stream material will have already moved far away from the region of impact and hence have little effect on the stream dynamics (in the pre-impact region) and the stream trajectory. It mainly affects the properties of the ambient matter (its composition and temperature) and hence the background conditions for the stream on a time-scale that is long compared to the stream infall time-scale (these effects and the associated nucleosynthesis can be followed with a standard stellar evolution code; see IP for a description of the nucleosynthesis calculations). The main effect of the nuclear burning on the stream hydrodynamics in this case is that the stream material, being affected by the nuclear burning, floats up faster and increases the efficiency of mixing in the core region. This decreases the density in the ambient medium around the stream and speeds up the establishment of a stationary stream.

The situation can be different when the stream impacts the core more-or-less radially and when the core has a very steep density gradient, causing a very strong shock and hence very high post-shock temperatures. This can lead to a nuclear runaway as illustrated in

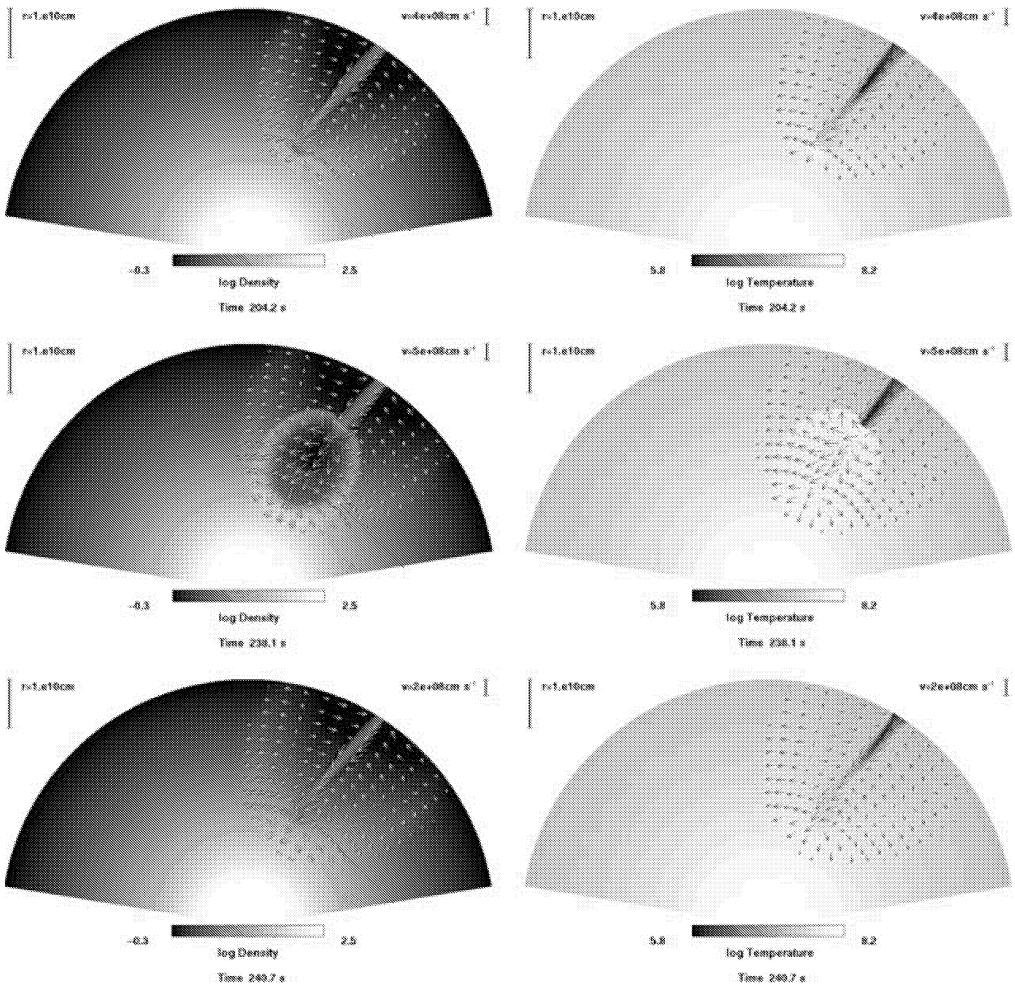

Figure 9. Density and temperature distributions for stream simulations illustrating the effect of violent nuclear ignition. The top two panels show the stream just before impact with the core and the point of nuclear ignition. The middle two panels show the detonation wave that develops shortly after nuclear ignition that disrupts the inflowing stream. The bottom two panels show a stream at the same time if nuclear burning is not included for comparison. The stream parameters are $M_{\rm int} = 9.9$, $M_{\rm ext} = 4$, $\eta_\rho = 7$, $R_{\rm T} = 5 \times 10^{10}$ cm, $R_{\rm s} = 0.03\pi$, $\Theta = 10^\circ$.

Fig. 9. As the middle panels in this figure show, it triggers a detonation wave that propagates up into the stream, almost completely disrupting it in the process. The expansion wave propagating into the ambient medium causes a dramatic expansion of the envelope material. Once all of the matter burning in this runaway has been consumed, one may expect that the stream re-establishes itself and that the process repeats, leading to pulsed nuclear burning.

6 THE PENETRATION DEPTH

6.1 The entropy change

In the idealized case of a stream of constant entropy, the depth of penetration can easily be estimated from the balancing of the stream ram pressure with the ambient pressure. In our case, the pressure of the stream material becomes comparable with the ambient pressure well before the stream reaches its deepest point. In this case it is better to use an estimate based on the conservation of the Bernoulli integral for matter along a streamline (though both estimates would give similar results). However, because the stream entropy changes because of the compression by shock waves propagating into the stream from the sides, one has to use a modified Bernoulli integral to estimate the penetration depth. This is possible as long as the stream is wide enough that it is not strongly affected by the K–H instability and that core rotation plays a minor role.

For this purpose, we rewrite the Bernoulli integral for stream material in the form:

$$\Phi_{\rm T} + \frac{u_{\rm S,T}^2}{2} + \frac{c_{\rm S,T}^2}{\gamma_{\rm S,T}-1} = \Phi_{\rm B} + \frac{u_{\rm S,B}^2}{2} + \frac{c_{\rm S,B}^2}{\gamma_{\rm S,B}-1}, \tag{24}$$

where u is the velocity of stream material, c the sonic speed of the stream material and Φ the potential. The subscript S corresponds to matter in the stream, the subscript T refers to the initial conditions and the subscript B refers to the conditions at the point of deepest penetration. The point of deepest penetration can then be determined by the condition that the pressure of the stream is equal to the pressure in the ambient matter and that the final stream velocity is zero (consistent with the results of our hydrodynamical calculations).

For the stellar structure parametrized by the pressure gradient, the corresponding potential can be written as

$$\Phi(r) = -\alpha_{\rm P}\frac{P(r)}{\rho(r)} = -\alpha_{\rm P}\frac{c_{\rm A}^2(r)}{\gamma_{\rm A}(r)}, \tag{25}$$

where the subscript A corresponds to the ambient matter at the initial point of the stream. Assuming that the entropy of the stream changes according to

$$\left(\frac{P}{\rho^\gamma}\right)_{\rm S,B} = K_{\rm S}\left(\frac{P}{\rho^\gamma}\right)_{\rm S,T}, \tag{26}$$

one can rewrite the Bernoulli integral to find $K_{\rm S}$ as a function of relative penetration depth, $\delta = r/r_{\rm T}$, and the initial conditions for the stream and ambient matter:

$$-\frac{\alpha_{\rm P}}{\gamma_{\rm A}} + \frac{M_{\rm ext}^2}{2} + \frac{M_{\rm ext}^2}{M_{\rm int}^2}\frac{1}{\gamma_{\rm S,T}-1} = -\frac{\alpha_{\rm P}}{\gamma_{\rm A}}\frac{\beta {\rm T}}{\beta(\delta)}\delta^{-\alpha_{\rm T}} + \frac{1}{\gamma_{\rm A}}\frac{\gamma_{\rm S,B}}{\gamma_{\rm S,B}-1}\left(K_{\rm S}\eta_\rho^{1-\gamma_{\rm S,T}}\rho_{\rm A}^{-\gamma_{\rm S,T}}\frac{M_{\rm ext}^2}{M_{\rm int}^2}\frac{\gamma_{\rm A}}{\gamma_{\rm S,B}}\right)^{\frac{1}{\gamma_{\rm S,B}}}\rho_{\rm A}\delta^{\frac{1}{\gamma_{\rm S,B}}-\alpha_{\rm P}}. \tag{27}$$

Here $\rho_{\rm A}$ is the density of the ambient material at the initial radius of the steam, and β is the ratio of gas pressure to total pressure for the ambient matter.

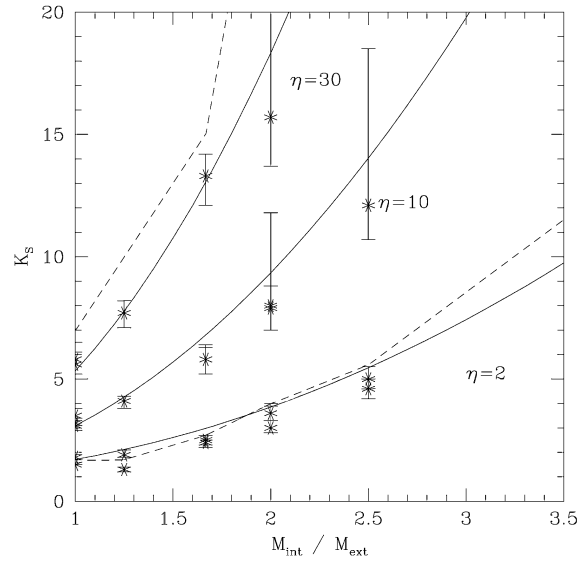

Figure 10. The entropy change as a function of the Mach numbers ratio for a parametrized ambient structure with $\alpha_{\rm P} = 5.2$ and $\alpha_{\rm T} = 1.3$. Asterisks correspond to values of $K_{\rm S}$ obtained from the hydrodynamical simulations by determining the appropriate value for $K_{\rm S}$ that would give the same penetration depth when using the Bernoulli integral as in the actual hydrodynamical simulation. The error bars are obtained by assuming an error in the determination of the penetration depth of 3 per cent. Solid curves correspond to the theoretical fit with $k = 0.45$, while the dashed curves show the change in entropy of the stream material in the hydrodynamical simulations.

6.2 Numerical fits

To determine the entropy change factor, $K_{\rm S}$, we performed sets of hydrodynamical simulations for two parametrized structures of the ambient medium, $(\alpha_{\rm P};\alpha_{\rm T}) = (5.2; 1.3)$ and $(4.2; 0.9)$, representing typical profiles in massive CE systems. We then calculated the stream penetration depth for 3 values of density ratios, $\eta_\rho = 2$, 10 and 30, and for a number of models with different Mach number ratios, $M_{\rm int}/M_{\rm ext}$ (where we varied $M_{\rm int}$, keeping $M_{\rm ext}$ fixed). All streams were calculated with an initial stream inclination of 18°.

Using the expression for a weak shock (equation 23), we fit the results to

$$K_{\rm S} = 1 + k(\alpha_{\rm P},\alpha_{\rm T})\,\eta_\rho^{\gamma-1}\left(\frac{M_{\rm int}}{M_{\rm ext}}\right)^2. \tag{28}$$

For an ambient medium, characterized by $\alpha_{\rm P} = 5.2; \alpha_{\rm T} = 1.3$, these results are well fitted by a constant $k = 0.4$ (see Fig. 10) and for a structure with $\alpha_{\rm P} = 4.2; \alpha_{\rm T} = 0.9$ by $k = 0.1$.

7 CONCLUSIONS

We have investigated the physics of the stream interaction with the core of a massive star in the phase where a star immersed in a common envelope merges with the core and systematically explored how the penetration depth depends on the initial properties of the stream and the core structure. For simulations representing the merger of a 1- and a 5-$M_\odot$ star with an evolved 20-$M_\odot$ supergiant, it typically penetrates to a depth of $1-3\times10^{10}$ cm, where it is being mixed vigorously with core material and is heated to temperatures $\gtrsim 10^8$ K. In the case of a slowly rotating core, the penetration depth mainly depends on the initial entropy and the entropy that is generated in the interaction. This also depends on the initial width of the stream (which is mainly a function of the mass-transfer rate), because

narrow streams are unstable to a Kelvin–Helmholtz instability. The main role of angular momentum in the stream is to determine the angle of incidence of the stream (which affects the dissipation in the stream). However, for a slowly rotating core, it is efficiently braked by the interaction with the core, spinning up the core in the process. In the case of a rapidly rotating core, the stream gains angular momentum from the core and the penetration is centrifugally limited. The stream behaviour is qualitatively and quantitatively different in the two cases. If the core is rotating slowly, the stream bounces off the core, quickly expanding away from the core, while in the case of a rapidly rotating core, the stream merges with the core in the form of a centrifugally supported ring.

In most cases, nuclear burning in the stream, which only becomes effective near the region of impact, does not affect the structure and dynamics of the stream itself, but modifies the ambient medium which changes the long-term evolution of the stream–core interaction. On the other hand, in the case of a very strong shock (in the case of a steep density gradient in the core and more or less normal incidence), shock-triggered nucleosynthesis can trigger a detonation wave that propagates upstream, temporarily disrupting the stream.

Using a simple model for the dissipation in a weak shock, we derived a simple recipe that allows the approximate determination of the penetration depth for a wide range of conditions. In a follow-up paper (IP), we will implement these results in a modified stellar-evolution code to model the whole merging phase of two stars in a slow merger.

REFERENCES

Colella P., Woodward P. R., 1984, J. Comp. Phys., 54, 174

Eggleton P. P., 1983, ApJ, 268, 368

Fryxell B. A., Müller E., Arnett W. D., 1989, MPA Report, 449. Max-Planck-Institut für Astrophysik, Garching

Garmany C. P., Conti P. S., Massey P., 1980, ApJ, 242, 1063

Ivanova N., Podsiadlowski Ph., Spruit H., 2001, in Podsiadlowski Ph., Rappaport S., King A. R., D'Antona F., Burderi L., eds, ASP Conf. Ser. Vol. 229, Evolution of Binary and Multiple Star Systems. Astron Soc. Pac., San Francisco, p. 261

Kahane C., Audinos P., Barnbaum C., Morris M., 1996, A&A, 314, 871

Kercek A., Hillebrandt W., Truran J. W., 1998, A&A, 337, 379 [KHT]

Kruszewski A., 1963, Acta Astron., 13, 107

LeVeque R. J., 1998, J. Comp. Phys., 146, 346

LeVeque R. J., Mihalas D., Dorfi E. A., Müller E., 1998, in Steiner O., Gautschy A., eds, Computational Methods for Astrophysical Fluid Flow. Springer, Berlin, p. 1

Limber D. N., 1963, ApJ, 138, 1112

Lubow S. H., Shu F. U., 1975, ApJ, 198, 383

Meyer F., Meyer-Hofmeister E., 1979, A&A, 78, 167

Paczyński B., 1976, in Eggleton P. P., Mitton S., Whelan J., eds, Structure and Evolution of Close Binaries. Kluwer, Dordrecht, p. 75

Paczyński B., Sienkiewicz R., 1972, Acta Astron., 22, 73

Podsiadlowski Ph., 1992, PASP, 104, 717

Podsiadlowski Ph., 1997, in SN 1987A, Ten Years After. CTIO/ESO/LCO Workshop, in press

Podsiadlowski Ph., 2001, in Podsiadlowski Ph., Rappaport S., King A. R., D'Antona F., Burderi L., eds, ASP Conf. Ser. Vol. 229, Evolution of Binary and Multiple Star Systems, p. 239

Podsiadlowski Ph., Rappaport S., Pfahl E., 2002, ApJ, 565, 1107

Rucinski S. M., 1990, PASP, 102, 306

Taam R. E., Sandquist E. L., 2000, ARA&A, 38, 113

Welty A. D., Ramsey L. W., 1994, ApJ, 435, 848

Zahn J.-P., 1975, A&A, 41, 329

Zeldovich Ya. B., Raizer Yu. P., 1966, Physics of Shock Waves and High-Temperature Hydrodynammics Phenomena. Academic Press, New York, pp. 45–68

This paper has been typeset from a TEX/LATEX file prepared by the author.